

Impact of magnetic anisotropy on the magnon Hanle effect in α -Fe₂O₃

M. Scheufele,^{1,2,a} J. Gückelhorn,^{1,2} M. Opel,¹ A. Kamra,³ H. Huebl,^{1,2,4} R. Gross,^{1,2,4} S. Geprägs,¹ and M. Althammer^{1,2,b}

¹⁾Walther-Meißner-Institut, Bayerische Akademie der Wissenschaften, 85748 Garching, Germany

²⁾Technische Universität München, TUM School of Natural Sciences, Physics Department, 85748 Garching, Germany

³⁾Condensed Matter Physics Center (IFIMAC) and Departamento de Física Teórica de la Materia Condensada, Universidad Autónoma de Madrid, 28049 Madrid, Spain

⁴⁾Munich Center for Quantum Science and Technology (MCQST), 80799 Munich, Germany

(Dated: 2 June 2023)

In easy-plane antiferromagnets, the nature of the elementary excitations of the spin system is captured by the precession of the magnon pseudospin around its equilibrium pseudofield, manifesting itself in the magnon Hanle effect. Here, we investigate the impact of growth-induced changes in the magnetic anisotropy on this effect in the antiferromagnetic insulator α -Fe₂O₃ (hematite). To this end, we compare the structural, magnetic, and magnon-based spin transport properties of α -Fe₂O₃ films with different thicknesses grown by pulsed laser deposition in molecular and atomic oxygen atmospheres. While in films grown with molecular oxygen a spin-reorientation transition (Morin transition) is absent down to 10 K, we observe a Morin transition for those grown by atomic-oxygen-assisted deposition, indicating a change in magnetic anisotropy. Interestingly, even for a 19 nm thin α -Fe₂O₃ film grown with atomic oxygen we still detect a Morin transition at 125 K. We characterize the magnon Hanle effect in these α -Fe₂O₃ films via all-electrical magnon transport measurements. The films grown with atomic oxygen show a markedly different magnon spin signal from those grown in molecular oxygen atmospheres. Most importantly, the maximum magnon Hanle signal is significantly enhanced and the Hanle peak is shifted to lower magnetic field values for films grown with atomic oxygen. These observations suggest a change of magnetic anisotropy for α -Fe₂O₃ films fabricated by atomic-oxygen-assisted deposition resulting in an increased oxygen content in these films. Our findings provide new insights into the possibility to fine-tune the magnetic anisotropy in α -Fe₂O₃ and thereby to engineer the magnon Hanle effect.

I. INTRODUCTION

The field of magnonics, utilizing the quantized spin excitations of magnetically ordered systems, i.e. magnons, offers a variety of interesting opportunities such as information processing with bosons and magnon-based computing approaches^{1–3}. Antiferromagnets are particularly appealing for magnonic logic devices due to their very fast magnetization dynamics in the THz regime and their robustness against external magnetic fields^{4–8}. Antiferromagnetic magnons come in pairs with opposite precession chiralities of the Néel order vector and thus opposite pseudospin^{9,10}. In the case of easy-plane antiferromagnets, linearly polarized spin waves with zero effective spin, which can be viewed as an equal superposition of basis states with opposite chirality, form the appropriate eigenmodes of the spin system^{11–15}. The manipulation and read-out of information encoded into antiferromagnetic magnons is demanding due to the vanishing stray fields of antiferromagnets. However, it has been demonstrated that this can be achieved by all-electrical magnon transport^{16–21}. There, the electrical injection and detection of magnonic spin transport is realized via two heavy-metal electrodes adjacent to the antiferromagnetic insulator by making use of the spin Hall and inverse spin Hall effect^{22–26}. In such

experiments the magnon Hanle effect, the analog of the electron Hanle effect, has been demonstrated in the easy-plane antiferromagnetic insulator α -Fe₂O₃. This has been achieved by a coherent control of the magnon pseudospin and long-distance magnon-based spin propagation in α -Fe₂O₃²⁴.

Bulk hematite (α -Fe₂O₃) is an antiferromagnetic insulator (AFI) below the Néel temperature $T_N = 953$ K and exhibits a spin-reorientation transition at the Morin transition temperature of $T_M = 263$ K²⁷. In the temperature range $T_M < T < T_N$, the magnetic moments are parallel to the magnetically easy α -Fe₂O₃ (0001)-plane as described by a uniaxial magnetic anisotropy along the [0001]-trigonal axis. Additionally, a finite spin canting is induced by the Dzyaloshinskii–Moriya interaction (DMI) resulting in a net magnetization of 2.5 kA m^{-1} perpendicular to the [0001] hard axis at room temperature^{27,28}. The easy-plane anisotropy gives rise to the magnon Hanle effect in α -Fe₂O₃ described by the precessional motion of antiferromagnetic magnon pseudospin around its equilibrium pseudofield oriented along the x -axis (see coordinate system in Fig. 2 (a))^{9,10}. For $T < T_M$, the uniaxial magnetic anisotropy reverses sign, leading to a reorientation of the magnetic Fe³⁺-moments along the [0001]-axis representing now the magnetically easy axis^{27,29}. In this easy-axis antiferromagnetic configuration, the net magnetization vanishes and one expects the magnon Hanle effect to disappear. This conjecture, however, is difficult to prove since films with small thickness are desirable in all-electrical magnon transport experiments to discern the magnon Hanle signature from the finite spin signal stemming from low energy magnons³⁰. However, in

^{a)} Author to whom correspondence should be addressed: monika.scheufele@wmi.badw.de

^{b)} Electronic mail: matthias.althammer@wmi.badw.de

thin α -Fe₂O₃ films with a thickness below 100 nm the Morin transition is usually suppressed as size-related effects change the delicate balance between magnetic-dipolar and uniaxial anisotropy contributions, which determines the Morin transition temperature^{31,32}. Therefore, the identification of growth conditions for α -Fe₂O₃ thin films, which show a Morin transition, are key for confirming the conjecture that an easy plane anisotropy is required for the presence of the magnon Hanle effect.

In this article, we investigate the crystallographic, magnetic and magnon transport properties of epitaxial α -Fe₂O₃ films with thickness values ranging from 15 nm to 124 nm. These films have been grown by pulsed laser deposition using two different growth atmospheres: (i) pure molecular oxygen and (ii) molecular oxygen with additional atomic oxygen. We observe a finite Morin transition temperature T_M in α -Fe₂O₃ films fabricated by atomic-oxygen-assisted deposition, while a Morin transition is absent in α -Fe₂O₃ films grown in molecular oxygen atmosphere. This suggests a modification of the magnetic anisotropy in α -Fe₂O₃ by changing the oxygen content. In all-electrical magnon transport measurements, the atomic-oxygen assisted growth of α -Fe₂O₃ yields a modification of the antiferromagnetic magnon pseudospin dynamics. Within the scope of the magnon Hanle effect, this manifests itself in an enhanced magnon spin signal amplitude and a shift of the Hanle peak towards smaller magnetic field magnitudes.

II. SAMPLE FABRICATION AND CHARACTERIZATION

Epitaxial α -Fe₂O₃ films are grown via pulsed laser deposition on (0001)-oriented, single crystalline sapphire (Al₂O₃) substrates. The growth process is carried out in an atmosphere of molecular oxygen with a partial pressure of 25 μ bar, while the substrate temperature is kept at 320 °C. The laser fluence at the polycrystalline α -Fe₂O₃ target is 2.5 J cm⁻² and the pulse repetition rate is set to 2 Hz³³. To reduce the formation of oxygen vacancies, we fabricated a second set of α -Fe₂O₃ films utilizing an atomic oxygen RF source (AOS) at a power of 400 W, where we add atomic oxygen to the deposition atmosphere, while all other deposition parameters are kept constant. In the following, we differentiate between NAOS-Fe₂O₃ films (no AOS used during deposition) and AOS-Fe₂O₃ films (AOS used during deposition). The thicknesses of the α -Fe₂O₃ films discussed in this article range from 15 nm to 124 nm to investigate the differences between NAOS- and AOS-Fe₂O₃ for both thin and thick films. Hereby, we consider α -Fe₂O₃ films as thin (thick), if the film thickness t_m is comparable to (much larger than) the thermal magnon wavelength l_{th} , which is typically much smaller than the magnon spin decay length. The thin and thick film limits and their influence on the magnon Hanle signal have been studied in detail in our previous work³⁰. The thickness values of the discussed α -Fe₂O₃ films are summarized in Table I.

We analyze the structural properties of our α -Fe₂O₃ films by high-resolution X-ray diffraction (HR-XRD) measurements. The corresponding 2θ - ω scans around the α -Fe₂O₃ (0006) film and Al₂O₃ (0006) substrate reflections are de-

TABLE I. Sample overview. The thicknesses are specified for the investigated α -Fe₂O₃ films analyzed by different measurement methods (see footnotes).

Atomic oxygen source used	thin α -Fe ₂ O ₃	thick α -Fe ₂ O ₃
No	15 nm ^{a,d}	103 nm ^{a,c,d}
No	25 nm ^{b,c}	124 nm ^b
Yes	19 nm ^{a,b,c,d}	89 nm ^{a,b,c,d}

^a 2θ - ω X-ray scan.

^b 2θ - ω X-ray scan and reciprocal space map (see supplementary material).

^c SQUID magnetometry.

^d All-electrical diffusive magnon transport.

picted in Fig. 1 (a), (b) for thin and thick α -Fe₂O₃ films, respectively. Thereby, we observe no secondary crystalline phases. Finite thickness fringes around the α -Fe₂O₃ (0006) reflections indicate a coherent growth and thus a good crystalline quality of the α -Fe₂O₃ films³⁴. Moreover, the (0006) reflections of the AOS-Fe₂O₃ films (black lines) are slightly shifted towards smaller 2θ -values with respect to the ones of the NAOS-Fe₂O₃ films (blue lines). This indicates an increase in the out-of-plane lattice constant c , when adding atomic oxygen to the fabrication process and thus reducing the oxygen deficiency in α -Fe₂O₃. Reciprocal space maps (RSMs) around the asymmetric α -Fe₂O₃ (10 $\bar{1}$ 10) and Al₂O₃ (10 $\bar{1}$ 10) reflections also confirm a slight reduction in c for AOS-Fe₂O₃ films, while the in-plane lattice constant a remains nearly constant. It should be mentioned that the changes in c are small and within the range of the measurement uncertainty. The extracted lattice parameters indicate a nearly relaxed growth of α -Fe₂O₃ on the Al₂O₃ substrates for all samples investigated. We obtain comparable values of the small, but finite epitaxial in-plane strain ϵ_{xx} for NAOS- and AOS-Fe₂O₃ films suggesting that the value of ϵ_{xx} is independent of the growth method. Furthermore, we do not observe any indication of an additional, strained α -Fe₂O₃ layer near the film-substrate interface due to clamping effects as stated in a recent publication³⁵. A detailed discussion on the RSMs and the extracted lattice constants is given in the supplementary material (SM).

To identify possible magnetic phase transitions in our α -Fe₂O₃ films, we performed superconducting quantum interference device (SQUID) magnetometry. After cooling the samples down to 10 K in zero field, we measured the magnetization M as a function of temperature T at a fixed magnetic field of $\mu_0 H = 100$ mT applied in the film plane. The corresponding results are presented in Fig. 1 (c) and (d), where a temperature-independent background signal was subtracted beforehand. This background signal is a linear function of $\mu_0 H$, which mainly stems from the diamagnetic Al₂O₃ substrate, but also from an increased sublattice canting in α -Fe₂O₃ with increasing $\mu_0 H$ ³⁴. The NAOS-Fe₂O₃ films exhibit no phase transitions over the whole temperature range from 300 K down to 10 K and thus remain in the magnetically (0001)-easy plane phase with a finite net magnetization induced by DMI. Generally, the shift of the Morin transition towards lower temperatures or its complete absence in α -Fe₂O₃ films can be attributed to strain-induced changes of the mag-

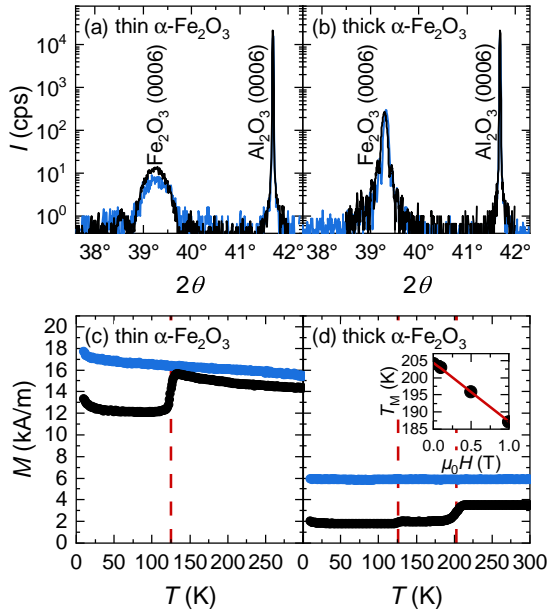


FIG. 1. Structural and magnetic properties of (a), (c) thin and (b), (d) thick α -Fe₂O₃ films measured by high-resolution X-ray diffraction (upper panels) and SQUID magnetometry (lower panels). Blue lines indicate α -Fe₂O₃ films deposited in molecular oxygen atmosphere (NAOS-Fe₂O₃ films) and black lines α -Fe₂O₃ films fabricated by atomic-oxygen-assisted deposition (AOS-Fe₂O₃ films). The 2θ - ω scans are performed around the α -Fe₂O₃ (0006) film and the Al₂O₃ (0006) substrate reflections. The α -Fe₂O₃ films have a thickness of (a) 15 nm (blue) and 19 nm (black) as well as (b) 103 nm (blue) and 89 nm (black). For the temperature-dependent magnetization measurements in (c) and (d), the same α -Fe₂O₃ films were investigated except for the thin NAOS-Fe₂O₃ film. Here, a 25 nm thin α -Fe₂O₃ film is utilized. The red, dashed vertical lines indicate the Morin transitions visible for the AOS-Fe₂O₃ films. All SQUID magnetometry measurements are conducted while heating the samples in an in-plane magnetic field of $\mu_0 H = 100$ mT after cooling down in zero field. The inset in (d) displays the extracted Morin transition temperature T_M as a function of the measurement field $\mu_0 H$ together with a linear fit in red.

netic anisotropy^{36–38}. However, as discussed above, all investigated α -Fe₂O₃ films are nearly relaxed and therefore exhibit only small in-plane strain values (see SM). At low temperatures, some of the α -Fe₂O₃ films show a small increase in M (cf. Fig. 1 (c)), which is most probably caused by paramagnetic moments within the Al₂O₃ substrate.

The AOS-Fe₂O₃ films, instead, reveal Morin transition temperatures of $T_M \approx 205$ K and $T_M \approx 125$ K for thick and thin films, respectively, which are found to decrease with increasing applied magnetic field (see inset of Fig. 1 (d)). As the small in-plane strain is comparable for NAOS- and AOS-Fe₂O₃ films, the absence (appearance) of the Morin transition in NAOS (AOS)-Fe₂O₃ can not be explained by strain-induced effects on the magnetic anisotropy. The atomic-oxygen-assisted deposition could rather lead to a reduction of oxygen vacancies and therefore to a change of the magnetic anisotropy in AOS-Fe₂O₃ films compared to the possibly more oxygen deficient NAOS-Fe₂O₃ films. We note

that an oxygen deficiency in the α -Fe₂O₃ films results in a partial reduction of Fe³⁺ to Fe²⁺ ions and thus is expected to change the magnetic anisotropy and T_M ³⁹. However, the Morin transition temperature of the AOS-Fe₂O₃ films is still smaller than in bulk crystals, which has also been recently reported for α -Fe₂O₃ thin films^{31,37}. Additionally, a second Morin transition at $T_M^* \approx 125$ K indicated by the small kink in the $M(T)$ curve can be observed for the thick AOS-Fe₂O₃ film (see Fig. 1 (d)). This low temperature Morin transition coincides with the single Morin transition in the thin AOS-Fe₂O₃ film and suggests that it originates from a region near the film-substrate interface with a different magnetic anisotropy. The detailed origin of the different magnetic anisotropy remains unknown. However, we can speculate that it is related to an increased defect density (e.g. oxygen vacancies) at the film-substrate interface, which affects the magnetic properties of our α -Fe₂O₃ films⁴⁰.

Although we expect a drop of M to zero for $T < T_M$ in the easy-axis phase, we observe a surprisingly large magnetization also for $T < 125$ K for the AOS-Fe₂O₃ films. Since we do not find any indications from HR-XRD for the presence of other iron oxide phases such as ferrimagnetic γ -Fe₂O₃ (maghemite) or Fe₃O₄ (magnetite) that could contribute to the finite magnetization of the samples, we suggest that the spin-reorientation at T_M is incomplete and leads to co-existing easy-plane and easy-axis phases in our AOS-Fe₂O₃ films below the respective Morin transitions. Notably, the net magnetization is larger in thin than in thick films, which can be induced by changes in the DMI, the exchange coupling or the magnetic anisotropy in α -Fe₂O₃. This observation is interesting and demonstrates that the impact of film thickness on the magnetic properties of the α -Fe₂O₃ films has to be taken into account and needs detailed consideration. In total, our SQUID magnetometry measurements suggest a more complex spin structure of our α -Fe₂O₃ films proving that an extensive study of the Morin transition can be a powerful tool to investigate the magnetic anisotropy in hematite films.

III. ALL-ELECTRICAL MAGNON TRANSPORT

In the following, we study the impact of different magnetic anisotropies induced by different oxygen atmospheres during the deposition of α -Fe₂O₃ films on their magnon transport properties. For our experiments, two 500 nm wide and 5 nm thick Pt strip electrodes with different center-to-center distances d (see Fig. 2 (a)) are patterned on top of the α -Fe₂O₃ films via lift-off process using electron-beam lithography and sputter deposition. We apply a DC charge current $I_{\text{inj}} = 500 \mu\text{A}$ to one Pt electrode injecting a spin current into the α -Fe₂O₃ film via the spin Hall effect (SHE)^{22–25}. The hereby excited diffusive pseudospin magnon current is electrically detected in the second electrode as a voltage signal V_{det} via the inverse SHE (iSHE)^{23,26}. We use the current reversal technique to extract the voltage signal $V_{\text{det}}^{\text{el}}$ originating from the SHE excited magnons^{17,41}. For fabrication and measurement details we refer to the SM. The electrically induced magnon spin signal $R_{\text{det}}^{\text{el}} = V_{\text{det}}^{\text{el}}/I_{\text{inj}}$ depends on the orienta-

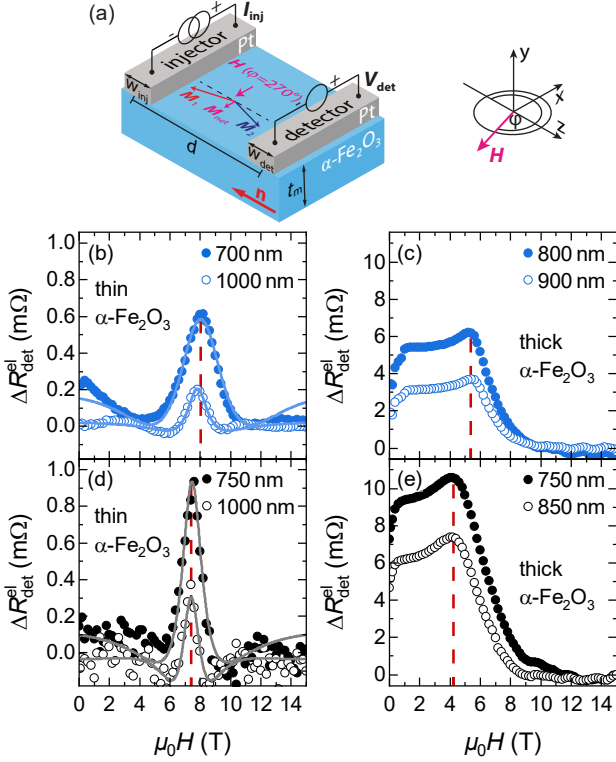


FIG. 2. (a) Scheme of the sample configuration consisting of two Pt strips on top of a α -Fe₂O₃ film in the magnetic (0001) easy-plane phase. The sublattice magnetizations \mathbf{M}_1 and \mathbf{M}_2 are slightly canted resulting in a net magnetization \mathbf{M}_{net} . The Néel order parameter $\mathbf{n} \perp \mathbf{M}_{\text{net}}$ is controlled by applying a magnetic field \mathbf{H} that is rotated in the film plane by the angle φ . A charge current is applied at the left Pt-electrode and the magnon spin signal is detected as a voltage at the right Pt-electrode. (b)-(e) Amplitude of the electrically induced magnon spin signal $\Delta R_{\text{det}}^{\text{el}}$ as a function of $\mu_0 H$ for thin (left panels) as well as for thick α -Fe₂O₃ films (right panels). The measurements are conducted at 200 K utilizing different injector-detector separations d (full and open circles). The 19 nm and 89 nm thick AOS-Fe₂O₃ films in (d) and (e) exhibit larger magnon spin signals than the 15 nm and 103 nm thick NAOS-Fe₂O₃ films in (b) and (c). The solid lines in (b) and (d) are fits to Eq. (1). The red, dashed lines indicate the compensation field $\mu_0 H_c$, where $\Delta R_{\text{det}}^{\text{el}}$ is maximum.

tion of the Néel vector \mathbf{n} with respect to the spin polarization \mathbf{s} of the injected spin current. The Néel vector is defined by the sublattice magnetizations \mathbf{M}_1 and \mathbf{M}_2 with corresponding saturation magnetizations M_1 and M_2 resulting in $\mathbf{n} = (\mathbf{M}_1/M_1 - \mathbf{M}_2/M_2)/2$. To orient the net magnetization $\mathbf{M}_{\text{net}} = \mathbf{M}_1 + \mathbf{M}_2$ and thus $\mathbf{n} \perp \mathbf{M}_{\text{net}}$, we apply a magnetic field \mathbf{H} in the film plane. We find $R_{\text{det}}^{\text{el}}$ to be maximum (zero) for $\mathbf{n} \parallel \mathbf{s}$ ($\mathbf{n} \perp \mathbf{s}$), which is the case for \mathbf{H} at $\varphi = 270^\circ$ (180°) (see coordinate system in Fig. 2 (a)).

This allows us to extract the electrically induced magnon spin signal amplitude $\Delta R_{\text{det}}^{\text{el}} = R_{\text{det}}^{\text{el}}(\varphi = 270^\circ) - R_{\text{det}}^{\text{el}}(\varphi = 180^\circ)$ that is shown in Fig. 2 (b)-(e) as a function of $\mu_0 H$ for different d (open and full circles). The measurements are conducted at 200 K, i.e. in the magnetic easy-plane phase of the NAOS-Fe₂O₃ films and of the thin AOS-Fe₂O₃ film ($T_M \leq 125$ K). In case of the thick AOS-Fe₂O₃ film, our

SQUID magnetometry results (inset in Fig. 1(d)) indicate that a magnetic field of 250 mT is large enough to shift T_M below 200 K and we maintain the easy-plane phase in the magnon transport experiments. In (b), the thin NAOS-Fe₂O₃ film exhibits the characteristic magnon Hanle curve, which is discussed in detail in our previous works^{10,30,42}. Note that $\Delta R_{\text{det}}^{\text{el}}$ is maximum at the so-called compensation field $\mu_0 H_c$ of about 8 T for both values of d . At $\mu_0 H_c$, the pseudofield ω is zero and hence the injected magnons propagate without any pseudospin precession¹⁰. The compensation field is therefore independent of the injector-detector distance and only depends on the material parameters of the hematite film. Furthermore, $\Delta R_{\text{det}}^{\text{el}}$ strongly decreases with increasing d , since the number of magnons carrying the spin current is not a conserved quantity, but decays within the magnon spin relaxation time τ_m . To quantify τ_m , we fit $\Delta R_{\text{det}}^{\text{el}}$ to the detectable z -component of the pseudospin chemical potential⁹

$$\mu_{sz} = \frac{l_m j_{s0} e^{-\frac{ad}{l_m}}}{D_m \chi (a^2 + b^2)} \left(a \cos\left(\frac{bd}{l_m}\right) - b \sin\left(\frac{bd}{l_m}\right) \right) \quad (1)$$

with $a, b = \sqrt{(\sqrt{1 + \omega^2 \tau_m^2} \pm 1)/2}$ and the magnon spin decay length $l_m = \sqrt{D_m \tau_m}$ (see SM for the extracted fit parameters). Here, j_{s0} is the magnon spin current density driven by the injector, D_m is the magnon diffusion constant and χ is the susceptibility relating the pseudospin density to the pseudospin chemical potential⁹. This fitting approach is only applicable for thin hematite films. In (c), the thick NAOS-Fe₂O₃ film reveals an offset in $\Delta R_{\text{det}}^{\text{el}}$ at magnetic fields below 5 T. This originates from the contribution of low-energy magnons, which become more dominant for increasing film thickness t_m ³⁰. Additionally, we observe an oscillating behavior of $\Delta R_{\text{det}}^{\text{el}}$ at high magnetic fields in agreement with our previous experiments³⁰. Compared to the thin NAOS-Fe₂O₃ film in (b), $\Delta R_{\text{det}}^{\text{el}}$ is one order of magnitude larger due to the higher density of magnonic states in thick α -Fe₂O₃³⁰. Furthermore, $\mu_0 H_c$ is shifted to a smaller magnetic field of 5.4 T, indicating a change in the magnetic anisotropy in thick α -Fe₂O₃ films.

The corresponding results of the thin and thick AOS-Fe₂O₃ films are presented in Fig. 2 (d) and (e). Clearly, the maximum value of $\Delta R_{\text{det}}^{\text{el}}$ is larger than for the NAOS-Fe₂O₃ counterparts shown in (b) and (c). Since the injector-detector distances of the respective NAOS- and AOS-Fe₂O₃ samples are comparable, the increased $\Delta R_{\text{det}}^{\text{el}}(\mu_0 H_c)$ for AOS-Fe₂O₃ cannot be explained by a decrease in d . Fits to Eq. (1) (see Fig. 2 (b), (d)) reveal a larger magnon spin decay length for the device with $d = 750$ nm on AOS-Fe₂O₃ than for the NAOS-Fe₂O₃ ($d = 700$ nm) sample. For the devices with $d = 1000$ nm, the extracted fit parameters suggest that the increased $\Delta R_{\text{det}}^{\text{el}}(\mu_0 H_c)$ for AOS-Fe₂O₃ originates from an increased factor j_{s0}/χ . As the measured spin Hall magnetoresistance (SMR) at the injector of all α -Fe₂O₃ samples is in the same order of magnitude (see SM), the larger $\Delta R_{\text{det}}^{\text{el}}(\mu_0 H_c)$ for AOS-Fe₂O₃ cannot be attributed to an enhanced spin current transparency of the α -Fe₂O₃/Pt interfaces, as it would also affect j_{s0} . Instead, the prefactor χ is reduced, which describes a change in the magnon density of states possibly due

to a change in the magnetic anisotropy of α -Fe₂O₃. Thus, a larger l_m as well as a smaller χ can explain the larger magnon Hanle peak signal for AOS-Fe₂O₃ films. In addition to the increase in $\Delta R_{\text{det}}^{\text{el}}(\mu_0 H_c)$, we observe a narrowing of the magnon Hanle peaks for the thin AOS-Fe₂O₃ film compared to the corresponding NAOS-Fe₂O₃ film (cf. Fig. 2 (b) and (d)). As the injector-detector distances of the respective NAOS- and AOS-Fe₂O₃ samples are comparable with each other, the fits to Eq. (1) suggest an increase in the fit parameter c_2 describing the magnetic field dependent contribution to the pseudofield $\omega = -c_1 + c_2 H$ and thus a change in the frequency of the pseudospin precession around its equilibrium pseudofield (see SM for details on the fitting procedure and extracted fit parameters)¹⁰.

Moreover, we observe a decrease in the compensation field $\mu_0 H_c$ to 7.4 T and 4.2 T for devices on thin and thick AOS-Fe₂O₃ films, respectively (see vertical dashed lines in Fig. 2 (d), (e)). At the compensation field $\mu_0 H_c$, the external magnetic field compensates the easy-plane anisotropy field in α -Fe₂O₃ resulting in a vanishing pseudofield¹⁰

$$\hbar\omega = \hbar\omega_{\text{an}} - \mu_0 m_{\text{net}} H_{\text{DMI}} = \hbar\tilde{\omega}_{\text{an}} - \mu_0 \tilde{m} H = 0 \quad (2)$$

with the easy-plane anisotropy $\hbar\omega_{\text{an}}$ and the reduced anisotropy energy $\hbar\tilde{\omega}_{\text{an}}$. The net magnetic moment is given by m_{net} and the DMI field by H_{DMI} , which is also taken into account by the magnetic moment \tilde{m} . The shift in $\mu_0 H_c$ for devices on AOS-Fe₂O₃ films is therefore associated with a change in the magnetic anisotropy in AOS-Fe₂O₃ with respect to the NAOS-Fe₂O₃ films (cf. Morin transitions in Fig. 1(c) and (d)). The decrease in $\mu_0 H_c$ is in agreement with the increase of T_M as we expect a reduced strength of the easy-plane anisotropy for the same T . Overall, we are able to tune the magnetic anisotropy and the magnon Hanle effect in α -Fe₂O₃ by adding atomic oxygen during the deposition process.

To further investigate the differences in $\Delta R_{\text{det}}^{\text{el}}$ between devices on NAOS-Fe₂O₃ and AOS-Fe₂O₃ films, we measure $\Delta R_{\text{det}}^{\text{el}}(H)$ at different temperatures ranging from 100 K to 300 K. The results are given in Fig. 3, where we focus on datasets for devices with fixed injector-detector distances for each α -Fe₂O₃ film. With increasing T , $\mu_0 H_c$ clearly shifts to higher magnetic fields as the magnetic anisotropy in α -Fe₂O₃ is temperature dependent²⁹. Moreover, $\Delta R_{\text{det}}^{\text{el}}$ at $\mu_0 H_c$ first increases with increasing T due to an increased amount of thermally occupied magnon states^{17,18}. In (b) and (c), however, the maximum of $\Delta R_{\text{det}}^{\text{el}}$ decreases again for $T > 250$ K as a result of an increase in magnon scattering processes³⁶. For the thin AOS-Fe₂O₃ film presented in Fig. 3 (c), no significant changes in $\Delta R_{\text{det}}^{\text{el}}(\mu_0 H)$ across the Morin transition temperature $T_M = 125$ K can be observed due to the low T_M , which further decreases for $\mu_0 H > 0$. In case of devices on the thick films, distinct differences in $\Delta R_{\text{det}}^{\text{el}}$ between devices on NAOS-Fe₂O₃ (Fig. 3 (b)) and on AOS-Fe₂O₃ films (Fig. 3 (d)) appear at $T \leq 150$ K. For $\mu_0 H < 4$ T, the plateau in $\Delta R_{\text{det}}^{\text{el}}$ originating from the contribution of low-energy magnons disappears in AOS-Fe₂O₃ and a peak-like behavior becomes visible instead (see Fig. 3 (d)). From the linear fit to $T_M(\mu_0 H)$ in the inset in Fig. 1 (d), we can conclude that at 150 K and at 100 K the AOS-Fe₂O₃ film is partially in the easy-axis phase

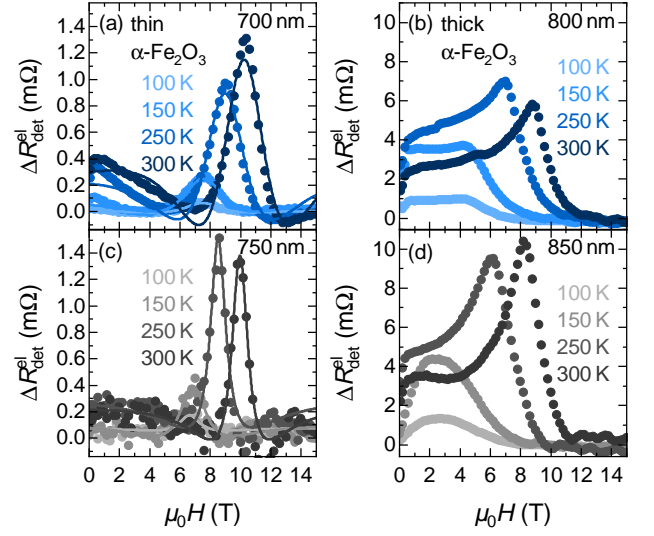


FIG. 3. Magnetic field dependence of the electrically induced magnon spin signal amplitude $\Delta R_{\text{det}}^{\text{el}}$ at different temperatures for (a) a $d = 700$ nm-device on a thin (15 nm) NAOS-Fe₂O₃ film, (b) a $d = 800$ nm-device on a thick (103 nm) NAOS-Fe₂O₃ film, (c) a $d = 750$ nm-device on a thin (19 nm) AOS-Fe₂O₃ as well as (d) a $d = 850$ nm-device on a thick (89 nm) AOS-Fe₂O₃ film. The solid lines in (a) and (c) are fits to Eq. (1).

for magnetic fields up to 3 T and 6 T, respectively. The peak-like behavior of $\Delta R_{\text{det}}^{\text{el}}$ is therefore in agreement with measurements in easy-axis α -Fe₂O₃, where it is attributed to a spin reorientation induced by the DMI⁴³.

We extract the compensation field $\mu_0 H_c$ and the electrically induced magnon spin signal amplitude $\Delta R_{\text{det}}^{\text{el}}$ at $\mu_0 H_c$ from the magnon Hanle curves recorded at different temperatures $100 \text{ K} \leq T \leq 300 \text{ K}$ and present both as functions of T in Fig. 4 (a)-(d). The compensation field exhibits the expected T^2 dependence for thin (a) as well as for thick α -Fe₂O₃ films (b)²⁹. Compared to the NAOS-Fe₂O₃ films (blue symbols), the respective compensation fields of the AOS-Fe₂O₃ films (black symbols) are reduced over the whole temperature range, but converge at higher temperatures. The thick AOS-Fe₂O₃ film (black in Fig. 4 (b)) exhibits the Morin transition at sufficiently large temperatures, below which the magnon Hanle effect simply vanishes. Correspondingly, $\mu_0 H_c$ and $\Delta R_{\text{det}}^{\text{el}}(\mu_0 H_c)$ can not be extracted for thick AOS-Fe₂O₃ at temperatures below 170 K. At $100 \text{ K} \leq T \leq 300 \text{ K}$, the amplitude $\Delta R_{\text{det}}^{\text{el}}(\mu_0 H_c)$ shown in Fig. 4 (c) and (d) is larger for AOS-Fe₂O₃ films than for NAOS-Fe₂O₃ films despite the slightly larger injector-detector distances for the AOS-Fe₂O₃ films. In addition, in (c) the maximum of $\Delta R_{\text{det}}^{\text{el}}(\mu_0 H_c)$ of AOS-Fe₂O₃ is shifted to lower T and in (d) to higher T compared to the NAOS-Fe₂O₃ films. Thus, the influence of magnon scattering at higher T strongly depends on the individual α -Fe₂O₃ film. Additional data for different d are provided in the SM and confirm the observed $\Delta R_{\text{det}}^{\text{el}}(T)$ behavior at $\mu_0 H_c$.

To investigate differences between NAOS- and AOS-Fe₂O₃ films in terms of the magnon spin decay length l_m , we extract l_m from the fits to Eq. (1) depicted in Fig. 2 (b) and (d)

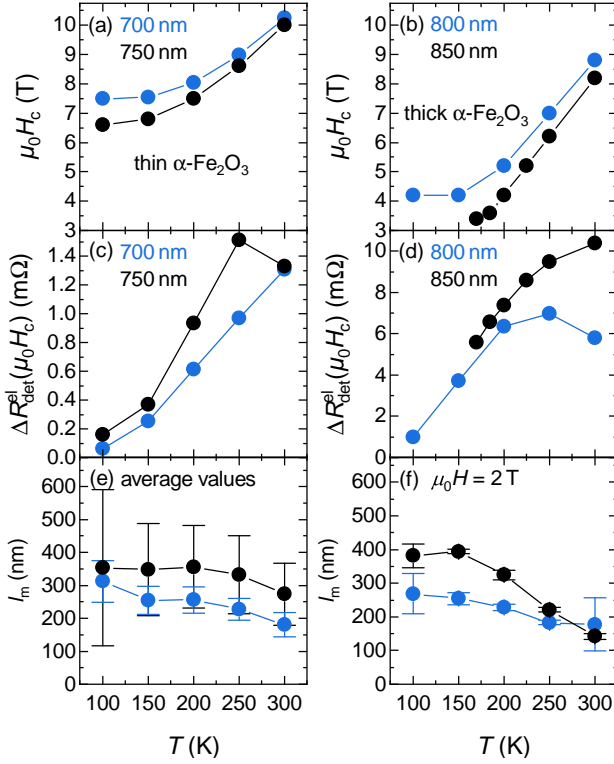


FIG. 4. (a), (b) Compensation field $\mu_0 H_c$, (c), (d) maximum detected spin signal amplitude $\Delta R_{\text{det}}^{\text{el}}(\mu_0 H_c)$ of the electrically excited magnons, and (e), (f) magnon spin decay length l_m as functions of temperature T . The left (right) panels correspond to thin (thick) α -Fe₂O₃ films and the blue (black) dots represent the NAOS (AOS)-Fe₂O₃ films. In (a)-(d), the injector-detector distances are given in the respective panels, whereas in (e) the average of l_m for different investigated injector-detector distances is given. In (f), l_m is taken at a magnetic field of 2 T by the fitting procedure described in the SM. The solid lines in (a)-(f) are guides to the eye.

and in Fig. 3 (a) and (c) for the thin α -Fe₂O₃ films. For the thick α -Fe₂O₃ films it is not possible to adequately fit $\Delta R_{\text{det}}^{\text{el}}(\mu_0 H)$. Therefore, we determine the magnon spin decay length of thick α -Fe₂O₃ by a different fitting procedure as described in the SM. In Fig. 4 (e) and (f), l_m is plotted as a function of T for thin and thick α -Fe₂O₃, respectively. Hereby in (e), we average over all investigated two-terminal devices with d ranging from 450 nm to 1300 nm depending on the respective thin film. In (f), l_m is determined at a magnetic field magnitude of 2 T, at which $\Delta R_{\text{det}}^{\text{el}}(\mu_0 H)$ exhibits a plateau above the Morin transition and a maximum below the Morin transition for thick α -Fe₂O₃. For thin as well as for thick α -Fe₂O₃ films, l_m first increases with decreasing T due to a reduction of magnon scattering processes. At lower T down to 100 K, l_m seems to saturate. In (e), the magnon spin decay length of NAOS-Fe₂O₃ is slightly reduced compared to the one of AOS-Fe₂O₃. However, taking into account the given uncertainties, l_m is approximately the same for NAOS- and AOS-Fe₂O₃ films. In (f), the magnon spin decay length of both α -Fe₂O₃ films is nearly the same for temperatures above 200 K. For $T \leq 200$ K, the magnon spin decay length of the

NAOS-Fe₂O₃ film is slightly smaller than for the AOS-Fe₂O₃ film. As we expect a partial reduction of Fe³⁺ to Fe²⁺ ions in oxygen deficient α -Fe₂O₃ films, the NAOS-Fe₂O₃ films could exhibit a higher density of Fe²⁺ ions than the AOS-Fe₂O₃ films, where the atomic-oxygen assisted deposition should enhance the oxygen content. Therefore, increased magnon scattering at Fe²⁺ ions could reduce the magnon spin decay length in NAOS-Fe₂O₃. All in all, the magnon spin decay length of the four investigated α -Fe₂O₃ samples is in the same order of magnitude, but slightly larger for AOS-Fe₂O₃. Hence, a change in the magnetic anisotropy affecting the effective susceptibility χ of the AOS-Fe₂O₃ films and the magnon spin decay length l_m in AOS-Fe₂O₃ is possibly causing the increase in the amplitude of the magnon Hanle peak.

IV. CONCLUSION

We fabricated α -Fe₂O₃ films of different thickness without (NAOS-Fe₂O₃) as well as with the addition of atomic oxygen during the deposition process (AOS-Fe₂O₃). We study the Morin transition in our samples, which is sensitive to the magnetic anisotropy in α -Fe₂O₃. The NAOS-Fe₂O₃ films exhibit no Morin transition down to 10 K, while the AOS-Fe₂O₃ films clearly show a Morin transition at around $T_M = 125$ K for the 19 nm thin and at around 205 K for the 89 nm thick film. This proves that we are able to tune the magnetic anisotropy and thus the Morin transition in thin as well as in thick α -Fe₂O₃ films using an atomic oxygen source. Furthermore, the thick AOS-Fe₂O₃ film reveals an additional Morin transition at 125 K, which indicates the existence of a second α -Fe₂O₃ phase with a different magnetic anisotropy near the film-substrate interface.

We conducted all-electrical magnon transport measurements above and below T_M and studied the magnon Hanle effect in our α -Fe₂O₃ films. Adding atomic oxygen during the growth process leads to two distinct changes: (i) an increase in the electrically induced magnon spin signal amplitude $\Delta R_{\text{det}}^{\text{el}}$ at the compensation field $\mu_0 H_c$ and (ii) a reduction of $\mu_0 H_c$. The increase in $\Delta R_{\text{det}}^{\text{el}}$ originates from an increase in the magnon spin decay length l_m or a decrease of the effective susceptibility χ describing a change in the magnon density of states. In addition, at $\mu_0 H_c$ the easy-plane anisotropy of α -Fe₂O₃ is compensated by the externally applied magnetic field. Therefore, the reduction of $\mu_0 H_c$ is consistent with the increase of T_M as for AOS-Fe₂O₃ the strength of the easy-plane anisotropy is reduced compared to the strength of the easy-axis anisotropy.

In summary, our results show that a variation of the oxygen content during the deposition process as well as a variation of the film thickness alters the magnetic anisotropy of α -Fe₂O₃. Our results provide a pathway towards a finite T_M in hematite films with thicknesses below 100 nm and a new perspective on the role of magnetic anisotropy for the magnon Hanle effect.

SUPPLEMENTARY MATERIAL

Additional XRD data, details on the fabrication and measurement methods and all-electrical magnon transport data are provided in the supplementary material. This includes reciprocal space mappings, calculated lattice constants as well as explanations on the fitting procedures, extracted fit parameters and further temperature dependent data.

ACKNOWLEDGMENTS

We gratefully acknowledge financial support from the Deutsche Forschungsgemeinschaft (DFG, German Research Foundation) under Germany's Excellence Strategy – EXC-2111 – 390814868, and the Spanish Ministry for Science and Innovation – AEI Grant CEX2018-000805-M (through the “Maria de Maeztu” Programme for Units of Excellence in R&D). This research is part of the Munich Quantum Valley, which is supported by the Bavarian state government with funds from the Hightech Agenda Bayern Plus.

AUTHOR DECLARATIONS

Conflict Of Interest

The authors have no conflicts to disclose.

Author Contributions

Monika Scheufele: Data curation (lead); Formal analysis (equal); Writing - original draft (lead). **Janine Gückelhorn:** Data curation (equal); Formal analysis (supporting); Investigation (lead); Writing - review & editing (supporting). **Matthias Opel:** Formal analysis (equal); Writing - review & editing (equal). **Akashdeep Kamra:** Formal analysis (supporting); Writing - review & editing (supporting). **Hans Huebl:** Writing - review & editing (supporting). **Rudolf Gross:** Funding acquisition (equal), Project administration (equal); Writing - review & editing (supporting). **Stephan Geprägs:** Conceptualization (equal); Data curation (supporting); Formal analysis (equal); Investigation (supporting); Project administration (equal); Supervision (lead); Writing - review & editing (equal). **Matthias Althammer:** Conceptualization (equal); Formal analysis (equal); Funding acquisition (equal); Project administration (equal); Supervision (supporting); Writing - review & editing (equal).

DATA AVAILABILITY

The data that support the findings of this study are available from the corresponding author upon reasonable request.

¹ A. V. Chumak, V. I. Vasyuchka, A. A. Serga, and B. Hillebrands, “Magnon spintronics,” *Nat. Phys.* **11**, 453–461 (2015).

- ² K. Nakata, P. Simon, and D. Loss, “Spin currents and magnon dynamics in insulating magnets,” *J. Phys. D* **50**, 114004 (2017).
- ³ M. Althammer, “All-Electrical Magnon Transport Experiments in Magnetically Ordered Insulators,” *Phys. Status Solidi - Rapid Res. Lett.* **15**, 2100130 (2021).
- ⁴ K. Olejník, T. Seifert, Z. Kašpar, V. Novák, P. Wadley, R. P. Campion, M. Baumgartner, P. Gambardella, P. Němec, J. Wunderlich, J. Sinova, P. Kužel, M. Müller, T. Kampfrath, and T. Jungwirth, “Terahertz electrical writing speed in an antiferromagnetic memory,” *Sci. Adv.* **4**, eaar3566 (2018).
- ⁵ P. Vaidya, S. A. Morley, J. van Tol, Y. Liu, R. Cheng, A. Brataas, D. Lederman, and E. del Barco, “Subterahertz spin pumping from an insulating antiferromagnet,” *Science* **368**, 160–165 (2020).
- ⁶ J. Li, C. B. Wilson, R. Cheng, M. Lohmann, M. Kavand, W. Yuan, M. Aldosary, N. Agladze, P. Wei, M. S. Sherwin, and J. Shi, “Spin current from sub-terahertz-generated antiferromagnetic magnons,” *Nature* **578**, 70–74 (2020).
- ⁷ T. Jungwirth, X. Marti, P. Wadley, and J. Wunderlich, “Antiferromagnetic spintronics,” *Nat. Nanotechnol.* **11**, 231–241 (2016).
- ⁸ V. Baltz, A. Manchon, M. Tsoi, T. Moriyama, T. Ono, and Y. Tserkovnyak, “Antiferromagnetic spintronics,” *Rev. Mod. Phys.* **90**, 015005 (2018).
- ⁹ A. Kamra, T. Wimmer, H. Huebl, and M. Althammer, “Antiferromagnetic magnon pseudospin: Dynamics and diffusive transport,” *Phys. Rev. B* **102**, 174445 (2020).
- ¹⁰ T. Wimmer, A. Kamra, J. Gückelhorn, M. Opel, S. Geprägs, R. Gross, H. Huebl, and M. Althammer, “Observation of Antiferromagnetic Magnon Pseudospin Dynamics and the Hanle Effect,” *Phys. Rev. Lett.* **125**, 247204 (2020).
- ¹¹ M. Kawano and C. Hotta, “Thermal Hall effect and topological edge states in a square-lattice antiferromagnet,” *Phys. Rev. B* **99**, 054422 (2019).
- ¹² M. W. Daniels, R. Cheng, W. Yu, J. Xiao, and D. Xiao, “Nonabelian magnonics in antiferromagnets,” *Phys. Rev. B* **98**, 134450 (2018).
- ¹³ L. Liensberger, A. Kamra, H. Maier-Flaig, S. Geprägs, A. Erb, S. T. B. Goennenwein, R. Gross, W. Belzig, H. Huebl, and M. Weiler, “Exchange-Enhanced Ultrastrong Magnon-Magnon Coupling in a Compensated Ferromagnet,” *Phys. Rev. Lett.* **123**, 117204 (2019).
- ¹⁴ R. Cheng, M. W. Daniels, J. G. Zhu, and D. Xiao, “Antiferromagnetic spin wave field-effect transistor,” *Sci. Rep.* **6**, 24223 (2016).
- ¹⁵ K. Shen, “Magnon Spin Relaxation and Spin Hall Effect Due to the Dipolar Interaction in Antiferromagnetic Insulators,” *Phys. Rev. Lett.* **124**, 077201 (2020).
- ¹⁶ L. J. Cornelissen, J. Liu, R. A. Duine, J. B. Youssef, and B. J. V. Wees, “Long-distance transport of magnon spin information in a magnetic insulator at room temperature,” *Nat. Phys.* **11**, 1022–1026 (2015).
- ¹⁷ S. T. B. Goennenwein, R. Schlitz, M. Pernpeintner, K. Ganzhorn, M. Althammer, R. Gross, and H. Huebl, “Non-local magnetoresistance in YIG/Pt nanostructures,” *Appl. Phys. Lett.* **107**, 172405 (2015).
- ¹⁸ L. J. Cornelissen, J. Shan, and B. J. van Wees, “Temperature dependence of the magnon spin diffusion length and magnon spin conductivity in the magnetic insulator yttrium iron garnet,” *Phys. Rev. B* **94**, 180402 (2016).
- ¹⁹ S. Vélaz, A. Bedoya-Pinto, W. Yan, L. E. Hueso, and F. Casanova, “Competing effects at Pt/YIG interfaces: Spin Hall magnetoresistance, magnon excitations, and magnetic frustration,” *Phys. Rev. B* **94**, 174405 (2016).
- ²⁰ S. S.-L. Zhang and S. Zhang, “Magnon Mediated Electric Current Drag Across a Ferromagnetic Insulator Layer,” *Phys. Rev. Lett.* **109**, 096603 (2012).
- ²¹ J. Li, Y. Xu, M. Aldosary, C. Tang, Z. Lin, S. Zhang, R. Lake, and J. Shi, “Observation of magnon-mediated current drag in Pt/yttrium iron garnet/Pt(Ta) trilayers,” *Nat. Commun.* **7**, 10858 (2016).
- ²² J. E. Hirsch, “Spin Hall Effect,” *Phys. Rev. Lett.* **83**, 1834–1837 (1999).
- ²³ J. Sinova, S. O. Valenzuela, J. Wunderlich, C. H. Back, and T. Jungwirth, “Spin Hall effects,” *Rev. Mod. Phys.* **87**, 1213–1260 (2015).
- ²⁴ R. Lebrun, A. Ross, S. A. Bender, A. Qaiumzadeh, L. Baldrati, J. Cramer, A. Brataas, R. A. Duine, and M. Kläui, “Tunable long-distance spin transport in a crystalline antiferromagnetic iron oxide,” *Nature* **561**, 222–225 (2018).
- ²⁵ S. O. Valenzuela and M. Tinkham, “Direct electronic measurement of the spin Hall effect,” *Nature* **442**, 176–179 (2006).
- ²⁶ E. Saitoh, M. Ueda, H. Miyajima, and G. Tatara, “Conversion of spin current into charge current at room temperature: Inverse spin-Hall effect,”

- Appl. Phys. Lett. **88**, 182509 (2006).
- ²⁷F. J. Morin, “Magnetic Susceptibility of $\alpha\text{Fe}_2\text{O}_3$ and $\alpha\text{Fe}_2\text{O}_3$ with Added Titanium,” Phys. Rev. **78**, 819–820 (1950).
- ²⁸A. H. Morrish, *Canted Antiferromagnetism: Hematite* (WORLD SCIENTIFIC, 1995).
- ²⁹P. J. Besser, A. H. Morrish, and C. W. Searle, “Magnetocrystalline Anisotropy of Pure and Doped Hematite,” Phys. Rev. **153**, 632–640 (1967).
- ³⁰J. Gückelhorn, A. Kamra, T. Wimmer, M. Opel, S. Geprägs, R. Gross, H. Huebl, and M. Althammer, “Influence of low-energy magnons on magnon Hanle experiments in easy-plane antiferromagnets,” Phys. Rev. B **105**, 094440 (2022).
- ³¹N. Shimomura, S. P. Pati, Y. Sato, T. Nozaki, T. Shibata, K. Mibu, and M. Sahashi, “Morin transition temperature in (0001)-oriented $\alpha\text{-Fe}_2\text{O}_3$ thin film and effect of Ir doping,” J. Appl. Phys. **117**, 17C736 (2015).
- ³²J. O. Artman, J. C. Murphy, and S. Foner, “Magnetic Anisotropy in Antiferromagnetic Corundum-Type Sesquioxides,” Phys. Rev. **138**, A912–A917 (1965).
- ³³J. Fischer, M. Althammer, N. Vlietstra, H. Huebl, S. T. Goennenwein, R. Gross, S. Geprägs, and M. Opel, “Large Spin Hall Magnetoresistance in Antiferromagnetic $\alpha\text{-Fe}_2\text{O}_3/\text{Pt}$ Heterostructures,” Phys. Rev. Appl. **13**, 014019 (2020).
- ³⁴S. Geprägs, M. Opel, J. Fischer, O. Gomonay, P. Schwenke, M. Althammer, H. Huebl, and R. Gross, “Spin Hall magnetoresistance in antiferromagnetic insulators,” J. Appl. Phys. **127**, 243902 (2020).
- ³⁵A. Wittmann, O. Gomonay, K. Litzius, A. Kaczmarek, A. E. Kossak, D. Wolf, A. Lubk, T. N. Johnson, E. A. Tremsina, A. Churikova, F. Büttner, S. Wintz, M.-A. Mawass, M. Weigand, F. Kronast, L. Scipioni, A. Shepard, T. Newhouse-Illige, J. A. Greer, G. Schütz, N. O. Birge, and G. S. D. Beach, “Role of substrate clamping on anisotropy and domain structure in the canted antiferromagnet $\alpha\text{-Fe}_2\text{O}_3$,” Phys. Rev. B **106**, 224419 (2022).
- ³⁶J. Han, P. Zhang, Z. Bi, Y. Fan, T. S. Safi, J. Xiang, J. Finley, L. Fu, R. Cheng, and L. Liu, “Birefringence-like spin transport via linearly polarized antiferromagnetic magnons,” Nat. Nanotechnol. **15**, 563–568 (2020).
- ³⁷K. Mibu, K. Mikami, M. Tanaka, R. Masuda, Y. Yoda, and M. Seto, “Thickness dependence of Morin transition temperature in iridium-doped hematite layers studied through nuclear resonant scattering,” Hyperfine Interact. **238**, 92 (2017).
- ³⁸S. Park, H. Jang, J.-Y. Kim, B.-G. Park, T.-Y. Koo, and J.-H. Park, “Strain control of Morin temperature in epitaxial $\alpha\text{-Fe}_2\text{O}_3$ (0001) film,” EPL **103**, 27007 (2013).
- ³⁹H. Jani, J. Linghu, S. Hooda, R. V. Chopdekar, C. Li, G. J. Omar, S. Prakash, Y. Du, P. Yang, A. Banas, K. Banas, S. Ghosh, S. Ojha, G. R. Umamathy, D. Kanjilal, A. Ariando, S. J. Pennycook, E. Arenholz, P. G. Radaelli, J. M. D. Coey, Y. P. Feng, and T. Venkatesan, “Reversible hydrogen control of antiferromagnetic anisotropy in $\alpha\text{-Fe}_2\text{O}_3$,” Nat. Commun. **12**, 1668 (2021).
- ⁴⁰O. Warschkow, D. E. Ellis, J. Hwang, N. Mansourian-Hadavi, and T. O. Mason, “Defects and Charge Transport near the Hematite (0001) Surface: An Atomistic Study of Oxygen Vacancies,” J. Am. Ceram. **85**, 213–220 (2002).
- ⁴¹K. Ganzhorn, S. Klingler, T. Wimmer, S. Geprägs, R. Gross, H. Huebl, and S. T. B. Goennenwein, “Magnon-based logic in a multi-terminal YIG/Pt nanostructure,” Appl. Phys. Lett. **109**, 022405 (2016).
- ⁴²J. Gückelhorn, S. de-la Peña, M. Scheufele, M. Grammer, M. Opel, S. Geprägs, J. C. Cuevas, R. Gross, H. Huebl, A. Kamra, and M. Althammer, “Observation of the Nonreciprocal Magnon Hanle Effect,” Phys. Rev. Lett. **130**, 216703 (2023).
- ⁴³A. Ross, R. Lebrun, O. Gomonay, D. A. Grave, A. Kay, L. Baldrati, S. Becker, A. Qaiumzadeh, C. Ulloa, G. Jakob, F. Kronast, J. Sinova, R. Duine, A. Brataas, A. Rothschild, and M. Kläui, “Propagation Length of Antiferromagnetic Magnons Governed by Domain Configurations,” Nano Lett. **20**, 306–313 (2020).